Available online at www.sciencedirect.com

SciVerse ScienceDirect

Ceramics International 39 (2013) 2365–2373

CERAMICS INTERNATIONAL

www.elsevier.com/locate/ceramint

Thermally activated sintering–coarsening–coalescence-polymerization of amorphous silica nanoparticles

Zih-Ling Chen, Pouyan Shen*

Department of Materials and Optoelectronic Science, National Sun Yat-sen University, Kaohsiung 80424, Taiwan, ROC

Received 9 August 2012; accepted 29 August 2012
Available online 5 September 2012

Abstract

An onset sintering–coarsening–coalescence-polymerization (SCCP) event of amorphous SiO_2 nanoparticles (ca. 40–100 nm in size) by isothermal firing in the 1150–1300 °C range in air was characterized by an N_2 adsorption–desorption hysteresis isotherm coupled with X-ray diffraction and vibrational spectroscopy. The apparent activation energy of such a rapid SCCP process was estimated as 177 ± 32 kJ/mol, based on 30% reduction of a specific surface area with an accompanied change of medium range orders, i.e. forming Si_2O_5 while retaining the Si–2ndO yet losing the Si–2ndSi without appreciable crystallization. The minimum temperature of the SCCP process, as of concern to industrial silica applications and sedimentary/metamorphosed sandstone formation, is 1120 °C based on the extrapolation of steady specific surface area reduction rates to null.

Keywords: Amorphous SiO_2; Coalescence; Coarsening; Early stage sintering

1. Introduction

Nanocrystalline powder compacts were known to reduce total surface area by the thermally activated processes of sintering, coarsening and coalescence [1–4]. Such processes occur readily for nanocrystals having relatively high specific surface area and high homologous temperature (T/T_m, where T_m is the melting point in Kelvin) given a lowered melting point [5] against the firing temperature. This has been experimentally proven for ionic oxide nanoparticles, such as equi-axed γ-Al_2O_3 [1], platy cobalt oxide [2], hexagonal rods of ZnO [3], and equi-axed ZrO_2 vs. the less refractory TiO_2 [4], based on electron microscopic observations coupled with BET/BJH measurements of specific surface area and pore size/shape changes of dry pressed samples subjected to isothermal firing at temperatures for minutes (BET and BJH denote the Brunauer–Emmett–Teller method [6] and Barrett–Joyner–Halenda method [7], respectively).

The specific-surface-area change rate in the steady state was used to determine the apparent activation energy of a vigorous onset sintering–coarsening–coalescence event for the above crystalline oxide nanoparticles [1–4]. A surprisingly low apparent activation energy for the ZrO_2 nanoparticles in comparison with that for less refractory and small-sized γ-Al_2O_3 nanoparticles was attributed to extensive polymorphic transformations of ZrO_2 for enhanced plasticity [4]. In addition, the minimum temperature for such processes to occur was estimated to be 516, 641 and 710 °C for nanosized ZnO [3], TiO_2 and ZrO_2 [4], respectively, based on the extrapolation of steady specific-surface-area reduction rates to null.

Here the BET/BJH method is further employed to study the onset sintering–coarsening–coalescence-polymerization (SCCP) of amorphous SiO_2 nanoparticles which have only 50% ionicity [8] and hence 40% higher bond strength (106 kcal/g-atom) than ionic oxides [9]. We focused on the activation energy and minimum temperature for incipient SCCP of the amorphous SiO_2 nanoparticles and the underlying effect, if any, of their structure change in terms of medium range order (MRO). This subject is of concern not only for the rapid assembly of SiO_2 nanocondensates by pulsed laser ablation (PLA) under the influence of radiant heating [10], but also for a number of industrial

*Corresponding author. Fax: +886 7 5254099.
E-mail address: pshen@mail.nsysu.edu.tw (P. Shen).

0272-8842/$ - see front matter © 2012 Elsevier Ltd and Techna Group S.r.l. All rights reserved.
http://dx.doi.org/10.1016/j.ceramint.2012.08.088

applications [11–14] and natural occurrences at high temperatures [15].

2. Experimental

The starting amorphous SiO_2 nanoparticles (UR ISIL001 99.8%) prepared by a sol–gel synthesis route were characterized by transmission electron microscopy (JEOL3010 at 200 kV) coupled with energy-dispersive X-ray analysis to be spherical, 40–100 nm in diameter and free of impurities (Appendix A). A fixed amount (0.06 g) of such SiO_2 nanoparticles was mixed with 1 wt% poly-vinyl alcohol (PVA) and then dry-pressed at 650 MPa into disks ca. 5 mm in diameter and 2 mm in thickness followed by isothermal firing at 1150–1300 °C for up to 60 min in air. The disks were fired in 10 min increments at 1150 °C but shorter increments (5, 3 or 1 min) at 1200, 1250 and 1300 °C in air until more than 70% reduction of the specific surface area was noted.

Microstructures of the dry-pressed and heat treated samples were studied by scanning electron microscopy (SEM, JEOL 6330 at 10 kV). The phase identity of each sample was determined by X-ray diffraction (XRD, CuKα; 40 kV, 30 mA at 0.05° and 3 s per step) in the 2θ range of 5°–50° and Raman spectra using laser excitation (633 nm) having a spatial resolution of 1 μm (HORIBA HR800). The pulverized samples were also mixed with KBr for Fourier transform infrared spectroscopy (FTIR, Bruker 66v/S, 64 scans in the range of ~400–4000 cm^{-1} with 4 cm^{-1} resolution) study of OH^- signature and structure unit changes of representative samples.

Nitrogen adsorption/desorption isotherms of the dry-pressed and then heated powders were conducted at a liquid nitrogen temperature of 77 K using a Micromeritics ASAP 2020 instrument. The surface area and pore size distributions were obtained from the N_2 adsorption and desorption branch, using the BET [6] and BJH method [7], in low and high relative pressure (P/P_o) range, respectively where P_o is the saturation pressure determined as ~760–762 mmHg. A filler rod containing the SiO_2 sample was pumped down to 10^{-3} Torr for degassing at 300°C followed by BET/BJH measurements at a relative pressure increment 0.05. The BET isotherm and BJH adsorption/desorption hysteresis type of the samples are classified according to the scheme of International Union of Pure and Applied Chemistry [16]. The H1 type adsorption/desorption hysteresis loop of the type IV isotherm (cf. Appendix A of Ref. [1]) was used as an indicator of cylindrical pore occurrence.

3. Results

3.1. BET/BJH observations of pore and specific surface area changes by firing

BET data of the fired samples indicated that the specific surface area decreases with an increase in dwelling time at a specific firing temperature for SiO_2 powders as compiled

Table 1
BET/BJH data and phase identity of 40–100 nm-sized amorphous SiO_2 powder subjected to various heating treatments.

T (°C)–t (min)	Specific surface area (m^2/g)	Ads./desorp. pore width (nm)	Phases
Dry-pressed	43.72	22.4/20.0	amp 1
1150–10	37.46	20.8/17.7	amp 2
1150–20	31.11	26.2/22.1	amp 2
1150–30	30.42	22.4/20.5	amp 2
1150–40	22.35	29.2/22.8	amp 2
1150–50	16.68	27.4/22.2	amp 2
1150–60	10.23	21.3/14.0	amp 2
1200–5	41.07	20.4/18.6	amp 2
1200–10	24.34	25.6/21.8	amp 2
1200–20	14.15	28.2/19.5	amp 2
1200–30	10.63	38.5/20.6	amp 2
1250–3	40.58	22.8/20.1	amp 2
1250–5	39.65	22.8/20.7	amp 2
1250–7	33.23	25.6/22.6	amp 2
1250–8	27.04	23.3/20.4	amp 2
1250–9	24.4	22.3/19.9	amp 2
1250–10	14.22	25.5/18.1	amp 2
1250–20	2.94	12.1/7.9	amp 2
1300–3	37.80	20.8/18.5	amp 2
1300–5	37.14	24.1/20.4	amp 2
1300–7	17.51	36.0/22.6	amp 2
1300–10	10.74	29.5/17.3	amp 2

Note: The abbreviation ads./desorp. denotes adsorption/desorption and the amorphous (amp) phases 1 and 2 have double (peaks at ca. 13° and 22°) and single (peak at ca. 22°) broad diffractions according to XRD. The crystalline silica phases, i.e. tridymite and cristobalite did not occur unless heated for a prolonged time, e.g. beyond 40 min at 1300 °C in the presence of PVA (Fig. 3).

in Table 1. By contrast, the average pore size shows a fluctuating increase with increase in dwelling time at a specific firing temperature.

The BJH N_2 adsorption-desorption hysteresis isotherms of the SiO_2 powders dry-pressed and further fired at 1150, 1200, 1250 and 1300 °C for specified time periods (Fig. 1a–d, respectively) show hysteresis loops in the relative pressure range 0.85–1.0 (i.e. actual pressure range ~648–762 mmHg). The dry-pressed sample has a H2 and H1 mixed type loop. The time to form a nearly perfect H1 type loop, as an indicator of cylindrical pore formation at all firing temperatures is vague. However, the time of specific surface area reduction to a certain percentage with respect to the dry-pressed sample can be unambiguously determined (Table 1). A longer firing time of up to 20 min at 1250 °C caused specific surface area reduction down to 2.94 m^2/g (Table 1) near the detection limit of BET and hence no loop in the adsorption–desorption hysteresis isotherm (Fig. 1c).

3.2. SEM observations of the sintered powder compacts

The cylindrical pores in the samples fired for a suitable time period at a specified temperature were observed by SEM, as shown in Fig. 2a–c, for 1150, 1200 and 1250 °C, respectively. Significant repacking and coalescence of slightly coarsened particles to form irregularly shaped islands were observed to be associated with the sintering process (Fig. 2b and c). The truncated pores and triple junction, an indicator of further coarsening/coalescence and solid-state sintering, were observed for the sample subjected to firing at 1300 °C for a prolonged time of 40 min (Fig. 2d). In such an extensively sintered case, microcracks were found to propagate along the grain boundaries and triple junctions, which are of concern to ceramic core applications as addressed later.

3.3. Structure change of amorphous SiO_2 upon firing

3.3.1. XRD

XRD indicated that the starting SiO_2 powder is amorphous with double broad diffraction peaks corresponding to MROs interspaced with 0.720 and 0.409 nm in real space (Fig. 3a). Upon firing within the temperature and time range for the present BET/BJH measurements, SiO_2 remained amorphous but with a significant MRO change to keep only the 0.409 nm broad diffraction peak. This is also the case of the SiO_2 sample fired at 1300 °C for a prolonged time of

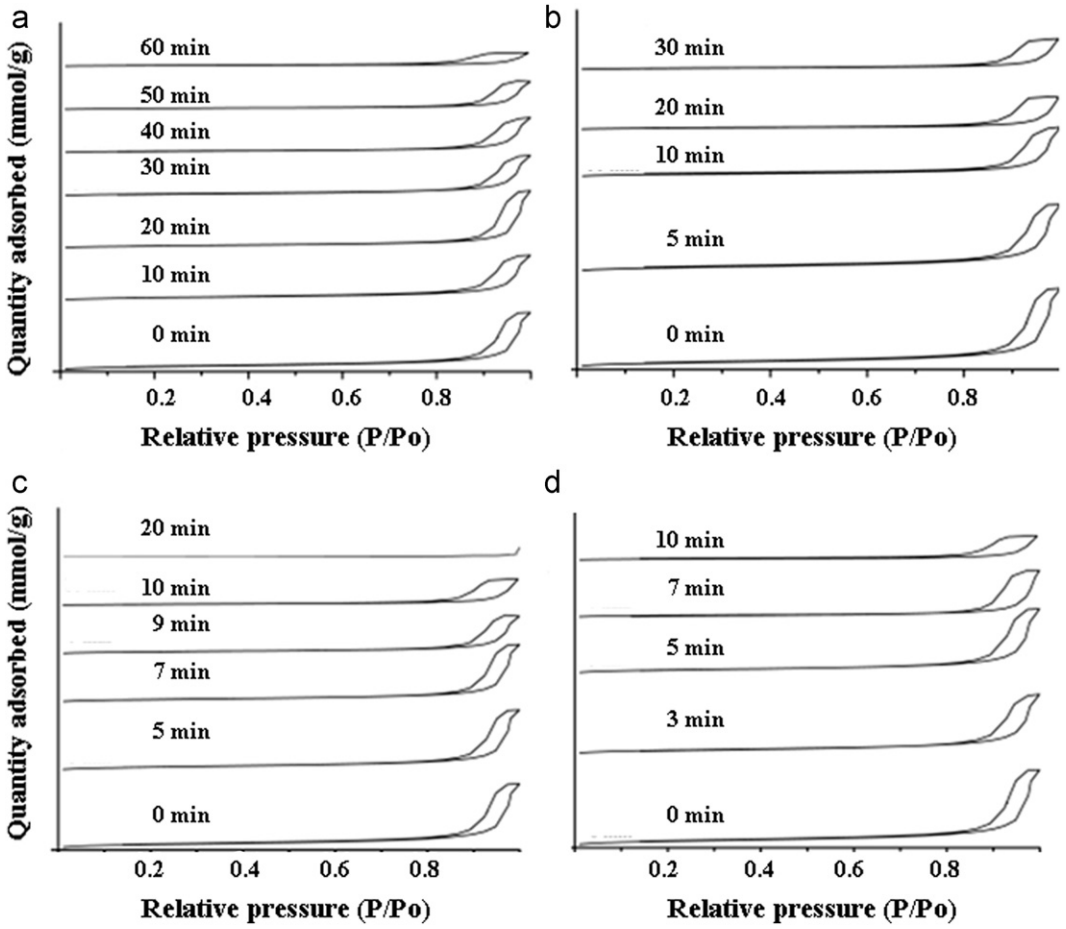

Fig. 1. BJH N_2 adsorption–desorption hysteresis isotherms of the SiO_2 powder dry-pressed with PVA binder and then subjected to the specified heat treatments: (a) 1150 °C for 0–60 min, (b) 1200 °C for 0–30 min, (c) 1250 °C for 0–20 min, and (d) 1300 °C for 0–10 min.

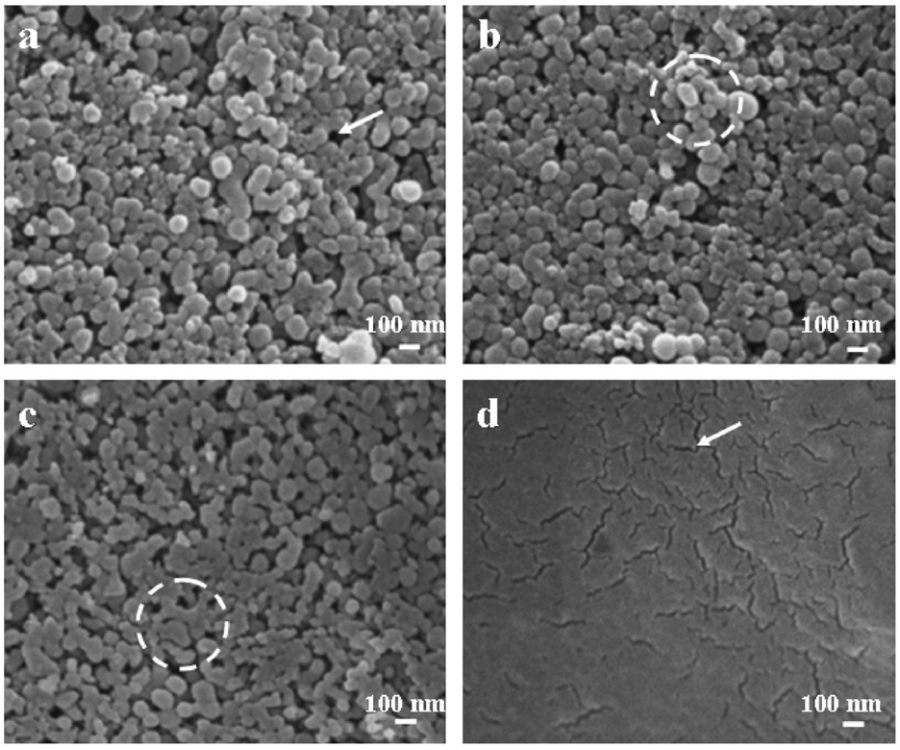

Fig. 2. SEM secondary electron images of the SiO_2 powder dry-pressed with PVA additive and then subjected to specified heat treatments: (a) 1150 °C, 60 min to show cylindrical pore (arrow), (b) 1200 °C, 30 min to show repacking of coarsened particles (circle), (c) 1250 °C, 7 min to show necking of repacked particles, and (d) 1300 °C, 40 min to show extensive microcracks with triple junction (arrow).

40 min in the absence of PVA additive (Fig. 3b). The PVA additive however caused partial crystallization of SiO_2 to form tridymite (JCPDS file 71-0197) and tetragonal cristobalite (JCPDS file 39-1425) under the same firing condition of 1300 °C and 40 min (Fig. 3c). Further firing for up to 60 min at 1300 °C caused more cristobalite formation at the expense of tridymite (Fig. 3d).

3.3.2. *Vibrational spectroscopy*

Raman spectrum of the starting amorphous SiO_2 powder shows weak Raman bands at 488, 604, and 806 cm^{-1} and a rather vague band near 1051 cm^{-1} (Fig. 4a). Such bands are presumably due to irregular vibrational structure units of 3- and/or 4-membered tertahedra rings corresponding to the two MROs observed by XRD. As for the samples fired at high temperatures, the above Raman bands are stronger and a new broad band, consisting of two bands peaked at 380 and 442 cm^{-1}, shows up in the 200–500 cm^{-1} range (Fig. 4b–d). The 442 cm^{-1} band along with the 488, 604, and 806 cm^{-1} bands can be attributed to the vibration of bridged SiO_4 units [17]. The 1051 cm^{-1} band corresponds to the Si_2O_5 units which are also present in amorphous zinc orthosilicate [18], whereas the 380 cm^{-1} band is due to microcrystalline opal-like units similar to that of tridymite [19].

The FTIR spectrum of the starting amorphous SiO_2 powder (Fig. 5a) shows a strong vibration near 1119 cm^{-1}, and two weaker bands at 808 and 476 cm^{-1} corresponding to asymmetric, symmetric and bending vibrations of silica bonds analogous to the case of vitreous silicate [20]. There are additional bands at 1637 and 3459 cm^{-1} due to bending and symmetrical vibration of water [21] indicating sol–gel-derivation of the starting SiO_2 powder. After firing, e.g. at 1300 °C for 10 min with PVA additive, the absorbance bands of silica became broadened and shift to lower wave numbers (Fig. 5b). It is noteworthy that the 469 and 795 cm^{-1} bands are much stronger (Fig. 5b) than the original 476 and 808 cm^{-1} bands (Fig. 5a) and the 1119 cm^{-1} peak shifts to 1105 cm^{-1} having a rather broad shoulder at higher wave numbers with longitudinal and transverse optical modes near the 1300–1000 cm^{-1} range. In addition, there are band slope breaks at 1643, 1882 and 2010 cm^{-1} (Fig. 5b) which can be attributed to SiH_x related vibrations [22], and/or Si–O bond angle/length changes [23]. The tiny bands at 2925 and 2845 $cm^{-1}$are the CH_2 vibrations due to ethanol used for FTIR sample preparation.

4. Discussion

4.1. *Thermally activated and PVA-assisted structure change of amorphous SiO_2*

Firing of gel-derived silica powders in air was accompanied by significant structure changes in terms of MRO, polymerization and crystallization. In general, MRO of an amorphous silica material with continuous random network [20,22] can be described by radiant parameters (r, k)

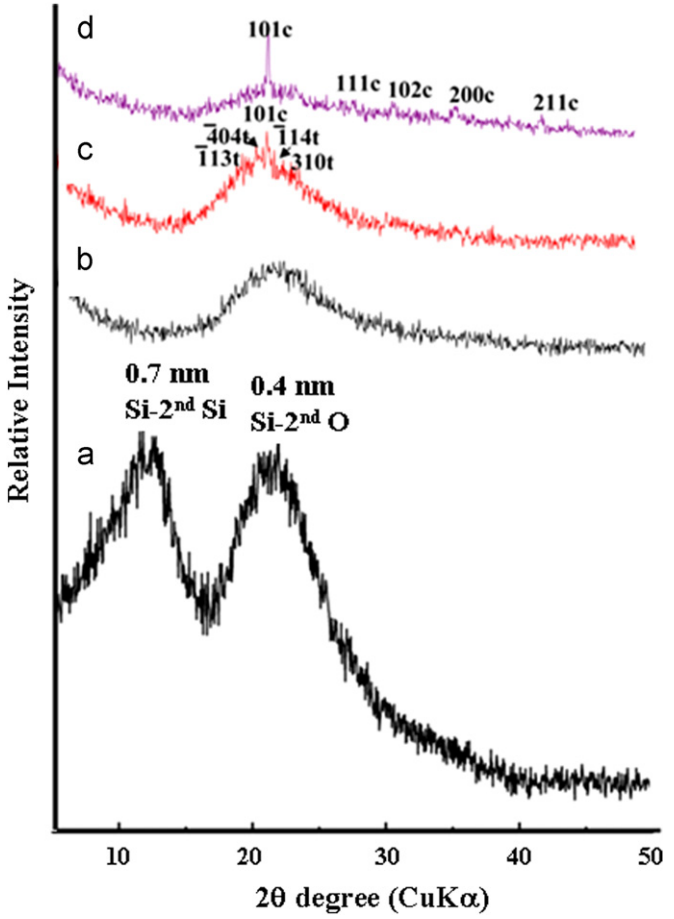

Fig. 3. XRD (CuKα) trace of (a) starting amorphous SiO_2 powder with double broad diffractions at low 2θ angle due to different medium range orders (cf. text), (b) amorphous SiO_2 with a single broad diffraction peak at ca. 22° 2θ after firing at 1300 °C for 40 min without PVA additive, (c) and (d) with PVA added and then fired at 1300 °C for 40 min and 60 min, respectively to form tridymite and then cristobalite (denoted as t and c, respectively).

and pair function distribution or quasi periodic model [24] in terms of corner-sharing of SiO_4 clusters to arrange atoms beyond the nearest neighbors. XRD indicated that the starting amorphous silica powders have two broad diffractions corresponding to the ~0.7 nm and ~0.4 nm average distances of Si–2ndSi and Si–2ndO, respectively [24]. By contrast, SiO_2 after firing in the present temperature and time ranges for BET/BJH measurements showed only ~0.4 nm average distance of the Si–2ndO unit, indicating that Si–2ndSi is significantly out of order by the firing process. Disordering could be due to SiO_4 distortion as a result of polymerization into Si_2O_5 units upon firing, as indicated by the enhanced Raman shift near 1051 cm^{-1} characteristic to such dimer units [18]. However the FTIR bands near 488 and 604 cm^{-1}, characteristic to symmetric oxygen ring breathing vibration of the three-membered ring (D_1) and four-membered ring (D_2), respectively, of fumed silica [17] and diatomaceous silica [25], remained after firing (Fig. 5).

It should be noted that enhanced hydrogenation of silica by the PVA additive upon firing in air, as manifested by

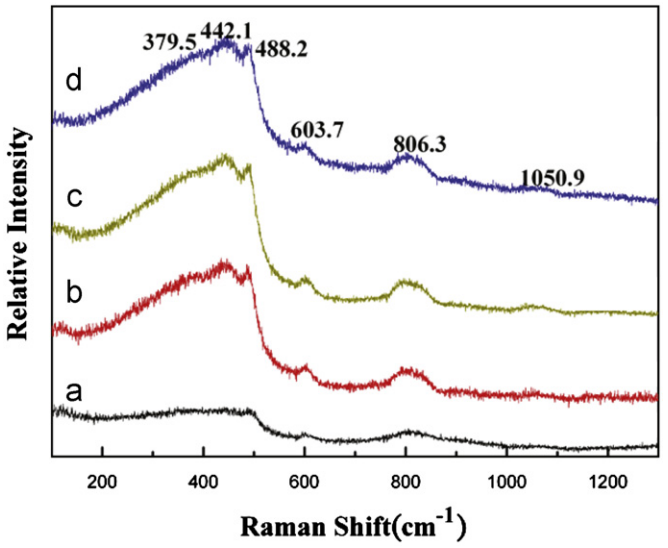

Fig. 4. Raman spectra of (a) starting amorphous SiO_2 powder and after specified heat treatments: (b) 1150 °C for 60 min (c) 1200 °C for 40 min, and (d) 1300 °C for 60 min.

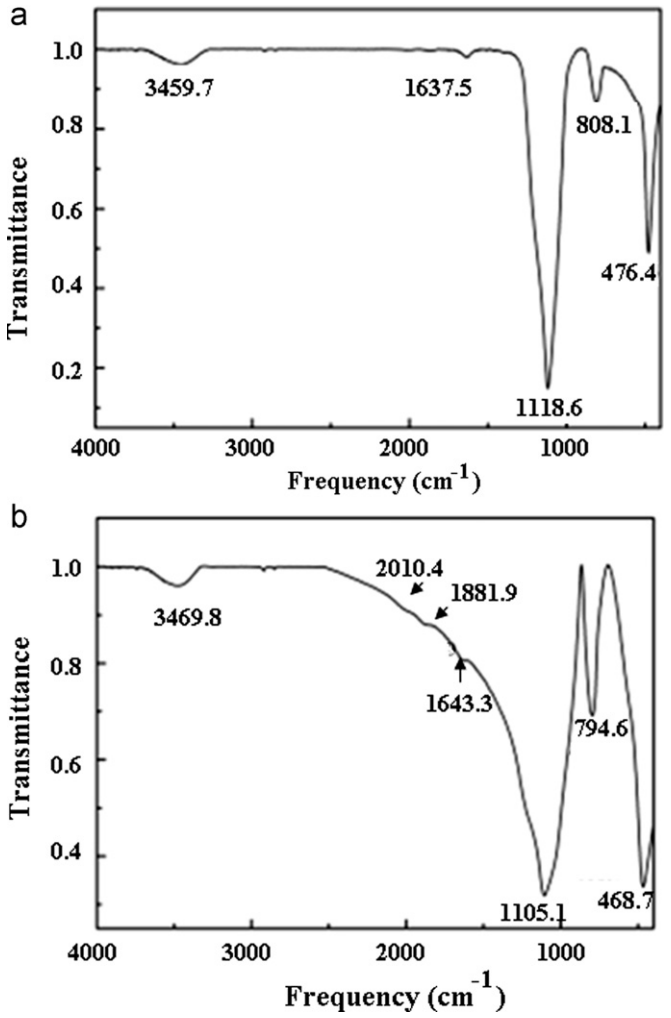

Fig. 5. FTIR spectra of (a) starting amorphous SiO_2 powder and (b) amorphous SiO_2 powder added with PVA and then fired at 1300 °C for 10 min.

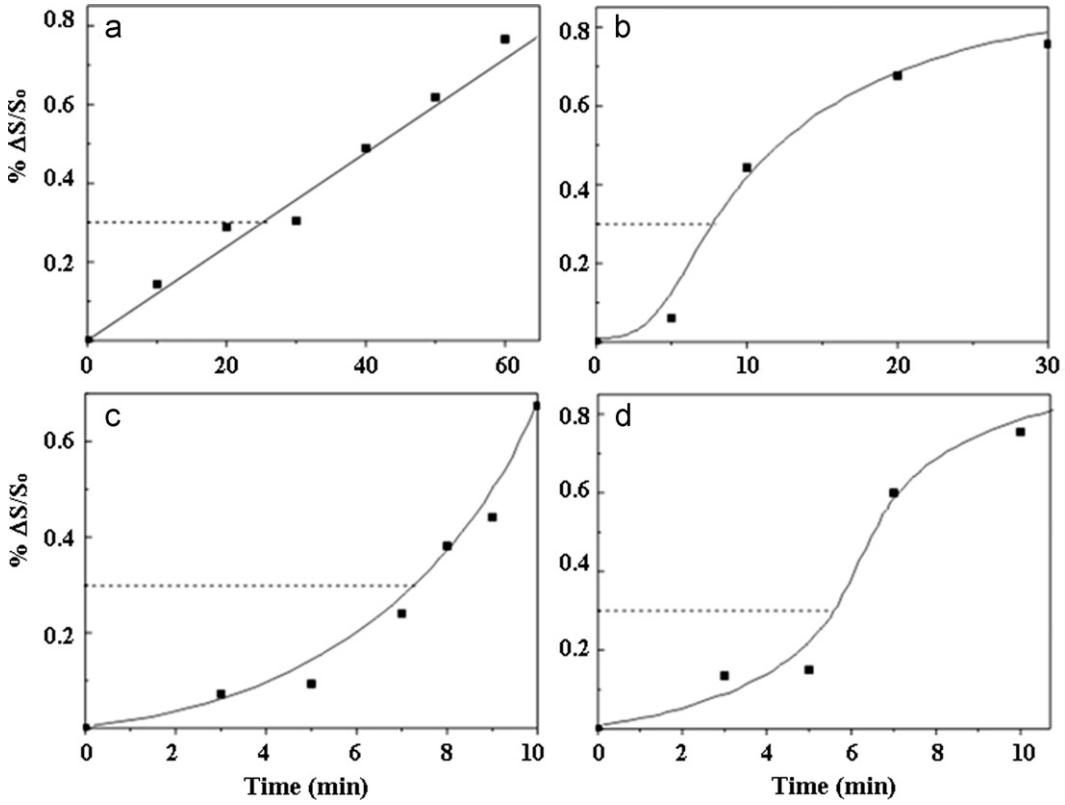

Fig. 6. Observed rate curves in terms of percentage reduction of specific surface area ($\Delta S/S_o$, where S_o is the initial quantity) vs. time for nanosized SiO_2 powder at specified temperatures: (a) 1150 °C, (b) 1200 °C, (c) 1250 °C, and (d) 1300 °C. The time $t_{0.3}$, i.e. with 30% reduction of specific surface area as denoted by dashed line, used for Activation energy estimation, falls within an almost linear region.

the broad FTIR absorbances at 1643, 1882 and 2010 cm^{-1} (Fig. 5b) due to SiH_x related vibrations [22], may also obliterate MRO analogous to the cases of hydrogenated amorphous semiconductor Si [26,27] and hydrogenated SiO_2 powder after PLA fragmentation in water [10]. Hydrogenation could also facilitate crystallization of the present SiO_2 nanoparticles to form tridymite and cristobalite at high temperatures as indicated by XRD results of the samples fired at 1300 °C for 40 min without vs. with PVA additive (Fig. 3b vs. c). In any case, crystallization is negligible for the samples fired in the temperature and time ranges for BET/BJH measurements in this study (Table 1).

4.2. Thermally activated SCCP of amorphous SiO_2 nanoparticles before crystallization

The present experimental results indicated that amorphous SiO_2 nanoparticles with more significant covalent bonding than metal oxides were thermally activated at a rather high homologous temperature range 0.72–0.80 (based on bulk $T_m \sim 1973$ K) in air for a vigorous surface area reduction event. By contrast, the ionic metal oxide nanoparticles were thermally activated at a lower homologous temperature range: 0.59–0.72 for γ-Al_2O_3 [1], 0.46–0.60 for TiO_2 and 0.32–0.42 for ZrO_2 under the additional influence of tetragonal→monoclinic transformation plasticity [4]. The apparent activation energy of the specific-surface-area reduction rate is essential to address the underlying SCCP mechanism of the present amorphous SiO_2 nanoparticles as follows.

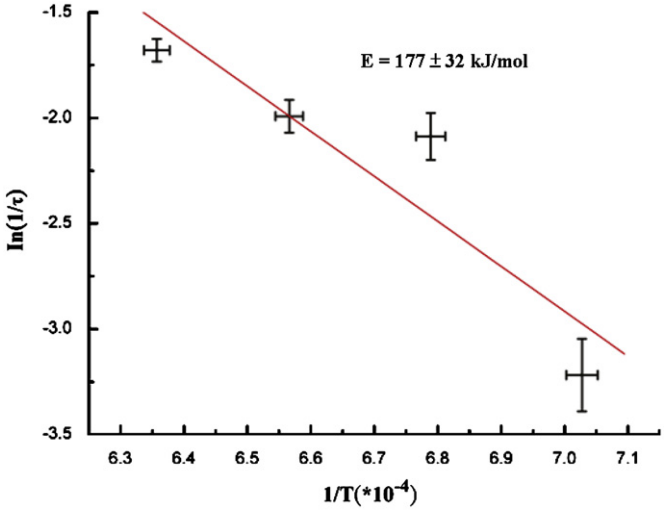

Fig. 7. Arrhenius plot of the logarithmic reciprocal time ($t_{0.3}$ in min) against reciprocal temperature (in Kelvin) for the specific surface area decrease by 30% from the dry-pressed SiO_2 nanoparticles with PVA additive.

On the basis of the drastic decrease of specific surface area by 30% (Table 1) in the linear region of the rate curves (Fig. 6), the onset time $t_{0.3}$ for SiO_2 powders for the onset SCCP process were determined. The onset time $t_{0.3}$ for amorphous SiO_2 with accompanied MRO change but no appreciable devitrification as crystalline phase (Table 1) turned out to be 25 ± 5, 8 ± 1, 7.0 ± 0.5 and 5.5 ± 0.5 min for 1150, 1200, 1250 and 1300 °C, respectively. The corresponding Arrhenius plot of the reciprocal time $t_{0.3}$ for onset SCCP vs. the reciprocal temperature in Kelvin gives an apparent activation energy 177 ± 32 kJ/mol considering the maximum uncertainty of each data point (Fig. 7). As a comparison, the metal oxide nanoparticles have lower activation energy for the sintering–coarsening–coarsening process: 119 ± 19 kJ/mol for γ-Al_2O_3 [1], 56 ± 3 kJ/mol for TiO_2 and 77 ± 2 kJ/mol for ZrO_2 under the additional influence of the transformation plasticity mentioned [4].

Brownian rotation of individual SiO_2 nanoparticles is expected to occur above a critical temperature higher than that for the diffusion of constituent atoms. This accounts for the rather limited reorientation and repacking of the nanoparticles at 1150 °C than the cases of higher temperatures (Fig. 2a vs. b and c). Sintering prevailing over the coarsening/coalescence process at 1150 °C also accounts for a much longer time (three times longer than at 1200 °C) to reach 30% reduction of the specific surface area. It cannot be excluded that the apparent activation energy of specific surface area reduction rate of the SiO_2 nanoparticles in the temperature range 1150°–1300 °C is actually controlled by the individual mechanisms of SCCP, i.e. predominant atom diffusion along the free surface and grain boundaries for sintering with a relatively high activation energy at 1150 °C and coarsening/coalescence of the nanoparticles with a relatively low activation energy above 1200 °C. However, it is difficult, if not impossible, to differentiate the underlying mechanisms in such a narrow temperature range under the present detection limit of BET. In any case the onset SCCP kinetics based on $t_{0.3}$ in this temperature range has nothing to do with the later crystallization of SiO_2.

4.3. Minimum temperature for vigorous SCCP of amorphous SiO_2 nanoparticles and its implications

The critical temperature (T_{cr}) for vigorous SCCP of amorphous SiO_2 nanoparticles is of concern to the preparation of SiO_2 nanoparticles or bulk assembly upon thermal exposure in a dynamic or static process. On the basis of the extrapolation of steady specific surface area reduction rates, i.e. those measured at $t_{0.3}$, to null (Fig. 8), T_{cr} is estimated as 1120 °C for the present 40–100 nm sized amorphous SiO_2 with PVA additive. This indicates that such sized SiO_2 nanoparticles are indeed able to sinter, coarse and coalesce coupled with considerable polymerization yet negligible crystallization under radiant heating in a dynamic PLA process [10].

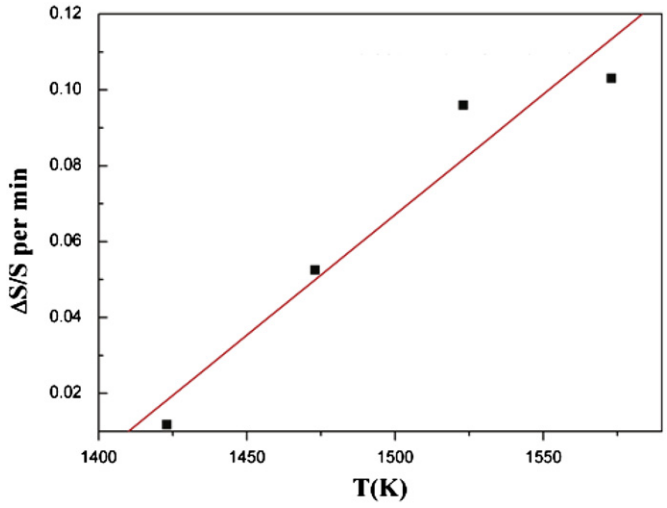

Fig. 8. Temperature dependent specific-surface-area reduction rate of the amorphous SiO_2 nanoparticles with PVA additive.

The T_{cr} and the extent of SCCP of the SiO_2 powder compact are of concern for the static firing of SiO_2 based ceramic cores toward a fair mechanical strength for casting superalloys [14]. In this connection, experimental coupled with mathematical modelings of SiO_2 crucibles used in production of solar panels has been conducted at slightly higher temperatures around 1250 °C, i.e. 1210, 1240 and 1270 °C [28]. However, the silica-based ceramic cores with additives can be sintered at a slightly lower temperature, e.g. near 900 °C having an α-cristobalite content kept below ca. 3 wt% after cooling to offer the optimal flexural strength at room temperature [14]. It should be noted also that when SiO_2 powders were extensively sintered at a relatively high temperature of 1300 °C, intergranular microcracks were introduced (Fig. 2d), presumably due to thermal mismatch of the individual grains under the combined effects of partial crystallization into tridymite and/or cristobalite, and the constraint of the compact powder when densified. The T_{cr} and activation energy of the SCCP process are also of great concern to SiO_2 aerogel dielectric [11] and mesoporous catalytic [12] applications at temperatures, SiO_2 glass preparation from powder compacts [13], as well as sedimentary and metamorphosed sandstone formation, such as the samples retrieved by the ocean drilling program [15].

5. Conclusions

1. BET/BJH adsorption–desorption hysteresis isotherms of nanosized amorphous SiO_2 with MRO were used satisfactorily to determine the time for the steady change of specific surface area as a characteristic of an onset SCCP event.
2. In the temperature range of 1150–1300 °C, the SiO_2 powder with PVA binder underwent onset sintering–coarsening–coalescence coupled with amorphous structure changes, i.e. forming Si_2O_5 units and retaining

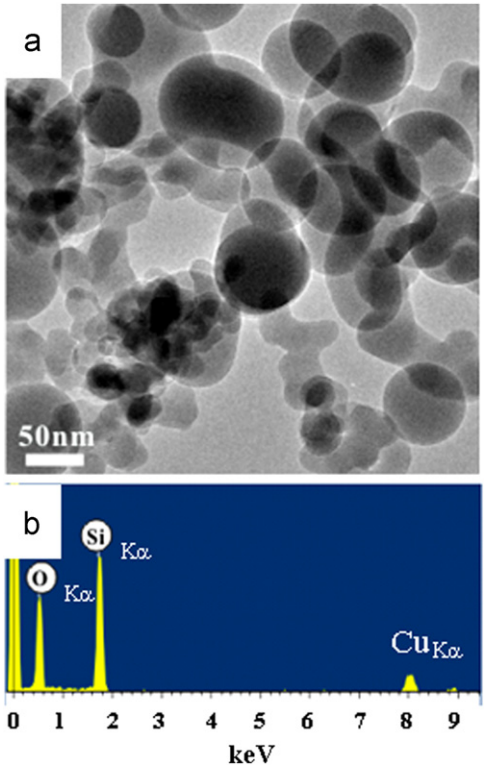

Fig. A1. TEM (a) BFI and (b) point count EDX of starting amorphous SiO_2 powder with poor diffraction contrast. The Cu counts are due to TEM specimen holder.

Si–2ndO yet losing Si–2ndSi MRO, before crystallization into tridymite and cristobalite.

3. The apparent activation energy for onset SCCP of amorphous SiO_2 nanoparticles was estimated as 177 ± 32 kJ/mol.
4. The minimum temperature for SCCP of the amorphous SiO_2 nanoparticles is 1120 °C based on the extrapolation of steady specific surface area reduction rates to null.

Acknowledgments

We thank Dr. S.Y. Chen for helpful discussion on the coalescence of nanoparticles in a dynamic PLA process. Supported by Center for Nanoscience and Nanotechnology at NSYSU and National Science Council, Taiwan, ROC.

Appendix A

See Fig. A1.

References

[1] I.L. Liu, P. Shen, Onset coarsening/coalescence kinetics of γ-type related Al_2O_3 nanoparticles: implications to their assembly in a laser ablation process, Journal of the European Ceramic Society 29 (2009) 2235–2248.

[2] Y. Yeh, I.H. Liu, P. Shen, Onset coarsening/coalescence of cobalt oxides in the form of nanoplates vs. equi-axed micron particles, Journal of the European Ceramic Society 30 (2010) 677–688.

[3] I.H. Liu, P. Shen, Coarsening, coalescence and sintering of hexagonal ZnO elongated nanoparticles, Ceramics International 36 (2010) 1289–1296.

[4] T.J. Chen, J.H. Lu, H.D. Lu, I.L. Liu, P. Shen, Onset coarsening–coalescence kinetics of ZrO_2 and less refractory TiO_2 nanoparticles: effect of homologous temperature and phase transformation, Journal of the European Ceramic Society 32 (2012) 795–805.

[5] A.N. Goldstein, C.M. Echer, A.P. Alivisatos, Melting in semiconductor nanocrystals, Science 256 (1992) 1425–1427.

[6] S. Brunauer, P.H. Emmett, E. Teller, Adsorption of gases in multimolecular layers, Journal of the American Chemical Society 60 (1938) 309–319.

[7] E.P. Barrett, L.G. Joyner, P.P. Halenda, The determination of pore volume and area distribution in porous substances I. Computations from nitrogen isotherms, Journal of the American Chemical Society 73 (1951) 373–380.

[8] A. Putnis, Introduction to Mineral Sciences, Cambridge Univ. Press, Cambridge, 1992.

[9] W.D. Kingery, H.K. Bowen, D.R. Uhlmann, Introduction to Ceramics, 2nd ed., John Wiley & Sons Inc., 1976.

[10] Z.L. Chen, C.H. Wu, P. Shen, S.Y. Chen, PLAL fragmentation of amorphous silica in water with optional NaCl spiking, Journal of Nanoscience and Nanotechnology 12 (2012) 1–9.

[11] M.H. Jo, H.H. Park, D.J. Kim, S.H. Hyun, S.Y. Choi, J.T. Paik, SiO_2 aerogel film as a novel intermetal dielectric, Journal of Applied Physics 82 (1997) 1299–1304.

[12] A. Sayari, in: P. Yang (Ed.), Mesoporous Materials, in the Chemistry of Nanostructured Materials, Word Scientific, New Jersey, 2003, pp. 39–68.

[13] M.D. Sacks, T.Y. Tseng, Preparation of SiO_2 glass from model powder compacts: I. Formation and characterization of powders, suspensions and green compact, Journal of the American Ceramic Society 67 (1984) 526–532.

[14] C. Huseby, M.P. Borom, C. Greskovich, High temperature characterization of silica-based cores for superalloys, American Ceramic Society Bulletin 58 (1979) 448–452.

[15] T. Vallier, L. Calk, R. Stax, A. Demant, Metamorphosed sedimentary (volcaniclastic?) rocks beneath basalt in Hole 917 A, East Greenland margin, in: A.D. Sanders, H.C. Larsen, S.W. Wise Jr., (Eds.), Proceedings of the Ocean Drilling Program, Scientific Results, 152 (1998) pp. 129–144.

[16] K.S.W. Sing, D.H. Everett, R.A.W. Haul, L. Moscou, R.A. Pierotti, J. Rouquerol, T. Siemieniewska, Reporting physisorption data for gas/solid systems with special reference to the determination of surface area and porosity, Pure and Applied Chemistry 57 (1985) 603–619.

[17] T. Uchino, A. Aboshi, S. Kohara, Y. Ohishi, M. Sakashita, K. Aoki, Microscopic structure of nanometer-sized silica particle, Physical Review B 69 (2004) 155409.

[18] C.C. Lin, P. Shen, Sol-gel synthesis of zinc orthosilicate, Journal of Non-crystalline Solids 171 (1994) 281–289.

[19] A. Ilieva, B. Mihailov, Z. Tsintsov, O. Petrov, Structural state of microcrystalline opals: a Raman spectroscopic study, American Mineralogist 92 (2007) 1325–1333.

[20] K. Kusabiraki, Y. Shiraishi, The infrared spectrum of vitreous fayalite, Journal of Non-Crystalline Solids 44 (1981) 365–368.

[21] A. Fidalgo, L.M. Ilharco, The defect structure of sol–gel-derived silica/polytetra–hydrofuran hybrid films by FTIR, Journal of Non-Crystalline Solids 283 (2001) 144–154.

[22] C. Tudisco, G.T. Sfrazzetto, A. Pappalardo, A. Motta, G.A. Tomaselli, I.L. Fragalà, F.P. Ballistreri, G.G. Condorelli, Covalent functionalization of silicon surfaces with a cavitand-modified salen, European Journal of Inorganic Chemistry 2011 (2011) 2124–2131.

[23] P. Innocenzi, P. Falcaro, D. Grosso, F. Babonneau, Order-disorder transition and evolution of silica structure in self-assembled mesostructured silica films studied through FTIR spectroscopy, Journal of Physical Chemistry B 107 (2003) 4711–4717.

[24] Y. Inaki, H. Yoshida, T. Yoshida, T. Hattori, Active sites on mesoporous and amorphous silica and their photocatalytic activity:

Investigations by FTIR, ESR, VUV–UV and photoluminescence spectroscopies, Journal of Physical Chemistry B 106 (2002) 9098–9106.
[25] P. Yuan, H.P. He, D.Q. Wu, D.Q. Wang, L.J. Chen, Characterization of diatomaceous silica by Raman spectroscopy, Spectrochimica Acta Part A 60 (2004) 2941–2945.
[26] J.M. Gibson, M.M.J. Treacy, P.M. Voyles, H.C. Jin, J.R. Abelson, Structural disorder induced in hydrogenated amorphous silicon by light soaking, Applied Physics Letters 73 (1998) 3093–3095.
[27] P.M. Voyles, M.M.J. Treacy, H.C. Jin, J.R. Abelson, J.M. Gibson, S. Guha, R.S. Crandall, Amorphous and heterogeneous silicon thin films, Conference Paper presented at the 2000 Spring Meeting of the Materials Research Society, San Francisco, CA, 24–28 April, 2000.
[28] U. Bethers, J. Sennikovs, H. Szillat, A. Timuhins, J. Virbulis, Mathematical modeling of sintering of SiO_2 crucibles, International Scientific Colloquium Modeling for Material Processing, Riga 8–9 (2006) 123–128.